



1 **A new approach for GNSS tomography from a few GNSS stations**

2

3 Nan Ding¹, Shubi Zhang¹, Suqin Wu², Xiaoming Wang³, Allison Kealy⁴, Kefei Zhang²

4 ¹ School of Environment Science and Spatial Informatics, China University of Mining and
5 Technology, Xuzhou, China

6 ² SPACE Research Centre, School of Mathematical and Geospatial Sciences, RMIT University,
7 Melbourne, Victoria, Australia

8 ³Academy of Opto-Electronics, Chinese Academy of Sciences, Beijing 100094, China

9 ⁴Geospatial Science, School of Science, RMIT University, Melbourne, Victoria, Australia

10

11 **Correspondence email:** metdingnan@163.com

12

13 **Abstract**

14 The determination of the distribution of water vapor in the atmosphere plays an important role in
15 the atmospheric monitoring. Global Navigation Satellite Systems (GNSS) tomography can be
16 used to construct 3D distribution of water vapor over the field covered by a GNSS network with
17 high temporal and spatial resolutions. In current tomographic approaches, a pre-set fixed
18 rectangular field that roughly covers the area of the distribution of the GNSS signals on the top
19 plane of the tomographic field is commonly used for all tomographic epochs. Due to too many
20 unknown parameters needing to be estimated, the accuracy of the tomographic solution degrades.
21 Another issue of these approaches is their unsuitability for GNSS networks with a few stations as
22 the shape of the field covered by the GNSS signals is in fact roughly an upside-down cone rather
23 than the rectangular cube as the pre-set. In this study, a new approach for determination of
24 tomographic fields fitting the real distribution of GNSS signals on different tomographic planes
25 at different tomographic epochs and also for discretization of the tomographic fields based on the
26 perimeter of the tomographic boundary on the plane and meshing techniques is proposed. The
27 new approach was tested using three stations from the Hong Kong GNSS network and validated
28 by comparing the tomographic results against radiosonde data from King's Park Meteorological
29 Station (HKKP) during the one month period of May, 2015. Results indicated that the new
30 approach is feasible for a three-station GNSS network tomography. This is significant due to the
31 fact that the conventional approaches cannot even solve a few stations network tomography.

32

33 **1 Introduction**

34 Information of the distribution and variation of atmospheric water vapor is essential for
35 meteorological applications. Nowadays, the most commonly used technology for measuring
36 atmospheric water vapor is radiosonde due to its high vertical resolution and high accuracy, even
37 though its horizontal resolution is very low—several hundreds of kilometers, and its temporal
38 resolution is also low—twice daily. With the development of Global Navigation Satellite Systems
39 (GNSS), using GNSS measurements to remotely sense water vapor in the atmosphere has



40 attracted significant attention due to their 24-hour availability, global coverage and low cost.
41 based on GNSS measurements collected from a regional or global GNSS reference network, a
42 regional or a global tomographic model, which is three-dimensional (3D), can be constructed.
43 The tomographic model reflects the spatial variation of water vapor in the time period
44 investigated, thus it has the potential to be used to investigate the evolution of heavy rain events
45 for severe weather forecast (Wang et al., 2017; Chen et al., 2017; Zhang et al., 2015).

46 Using the slant wet delays (SWDs) estimated from the GNSS signals of a GNSS network
47 to construct a tomographic model is called GNSS tomography. Flores et al. (2000) built the first
48 GNSS tomographic model using $4 \times 4 \times 40$ voxels and developed Local Tropospheric Tomography
49 Software (LOTTOS) for simulation and processing of GNSS data. Gradinarsky (2002) developed
50 the wet refractivity Kalman filter (WeRKaF) for tomographic inversion of GNSS data and the
51 filter mainly focused on the initialization of the tomographic covariance matrix used in the
52 implementation of the Kalman filter. Troller et al. (2006) developed the atmospheric water vapor
53 tomography software (AWATOS) based on double-differenced GPS observations and double-
54 differenced phase residuals. Rohm and Bosy (2009) addressed the issue with the ill-condition of
55 tomographic equations using the Moore-Penrose pseudo inverse of the variance-covariance
56 matrix. In order to minimize the discretization effects, Perler et al. (2011) for the first time
57 proposed using node parameterization in GNSS tomographic modeling. Chen and Liu (2014)
58 optimized a water vapor tomographic region through moving voxel location along the latitudinal
59 and longitudinal directions until the number of the voxels that contain GNSS signals reached the
60 maximum. Yao et al. (2016) improved the utilization rate of GNSS observations in the modeling
61 by adding extra voxels on the top of the tomographic region where some satellite signals partly
62 cross the tomographic field. Ding et al. (2017) developed an access order scheme called prime
63 number decomposition (PND) for minimizing the correlation between the SWDs which are the
64 sample data of tomographic modeling. The above GNSS tomographic approaches were tested
65 using various numbers of GNSS stations, majority of which were a few tens of stations, and the
66 maximum and minimum were 270 and 8 respectively.

67 In all the above tomographic approaches, the tomographic fields are all assumed
68 rectangular cubes. The size and location of the rectangular cubes are determined based on the
69 distribution of GNSS signals only on the top boundary of the tomographic field—the rectangular
70 cube that best fits the top boundary is adopted (Bastin et al., 2005; Bender et al., 2009;
71 Champollion et al., 2005; Ding et al., 2017; Gradinarsky and Jarlemark, 2004; Hoyle, 2005;
72 Rohm et al., 2014; Seko et al., 2000; Troller et al., 2006; Xia et al., 2013; Ye et al., 2016). In fact,
73 the field that GNSS signals cover has a shape of upside-down cone, roughly, meaning that in the
74 part near the edge of the cube, especially in the lower part, none of the GNSS signals cross
75 through. This region is named empty spatial region (ESR) in this paper merely for convenience.
76 In fact, the inclusion of those voxels/nodes in the ESR in the discretization of the model not only
77 does little contribution to the improvement on the accuracy of the model solution but also adds
78 extra meaningless unknown parameters to be estimated. More parameters mean more horizontal
79 constraints are needed and also degradation of the accuracy and stability of the solution,
80 especially in the case the network consists of a few stations, e.g. only three stations. This is
81 because the difference in the sizes covered by the GNSS signals in the bottom and top planes of
82 the tomographic field is large, meaning a large number of voxels/nodes in the ESR and far away
83 from the observed signals, especially in the lower part of the tomographic field. In the estimation
84 process of the model, the horizontal constraints imposed on these nodes/voxels are usually from
85 extrapolated results based on their nearest observations. If these voxels/nodes are far away from



86 the observed signals, the constraints are too weak and will cause difficulty in the solving of the
87 tomographic equations. The large number of nodes/voxels contained in ESRs stemming from a
88 small number of GNSS stations is the main reason for the unsuitable of the current GNSS
89 tomographic approaches to using a-few-station networks.

90 In this study, a new node parameterization approach for dynamic determination of
91 tomographic fields and the discretization of the fields at each tomographic epoch was proposed.
92 It is adaptive node parameterization for varying density on different tomographic planes. This
93 differs from all current approaches in which the same pre-set rectangular cube roughly
94 determined by the distribution of the signals only on the top tomographic plane is adopted for all
95 planes and all epochs of the tomography. In addition, for the discretization of the tomographic
96 field determined for each plane at each epoch, the location and number of all the nodes on the
97 plane are determined according to the size of the tomographic field. As a result, the tomographic
98 model is tailor-made for all planes and all epochs. Moreover, the new approach is applicable to
99 GNSS networks with any number of stations, i.e. equal to or larger than three.

100 **2 Methodology**

101 2.1 Observations of GNSS Tomography

102 GNSS signals are bent and delayed when they propagate through the atmosphere. The
103 atmosphere can be divided into the ionosphere and troposphere. The ionospheric delay can be
104 cancelled out using an ionosphere-free linear combination of dual-frequency observations. The
105 tropospheric delay can be divided into two components—the dry delay and the wet delay. The wet
106 component is the SWD and can be expressed by

$$107 \quad SWD = m_w(e) \cdot \left\{ ZWD + \left[G_N^w \cdot \cos(\phi) + G_E^w \cdot \sin(\phi) \right] \cdot \cot(e) \right\} + R \quad (1)$$

108 where $m_w(e)$ is a wet mapping function and the VMF1 mapping function was used in this study;
109 G_N^w and G_E^w are the wet delay gradients in the north–south and east–west directions, respectively;
110 R is the unmodeled delay; ZWD is the zenith wet delay of the GNSS station, which can be
111 obtained by subtracting the zenith hydrostatic delay (ZHD) from the zenith total delay (ZTD).
112 The ZHD can be calculated by a standard tropospheric model such as the most commonly used
113 Saastamoinen model (Saastamoinen, 1972) and the ZTD is estimated (as an unknown parameter)
114 in GNSS data processing;

115 In GNSS tomographic modeling, the SWDs of GNSS signals in a tomographic field are
116 used as the observations for the estimation of water vapor parameters in the field.

117 2.2 Tomographic modeling

118 2.2.1 General approaches

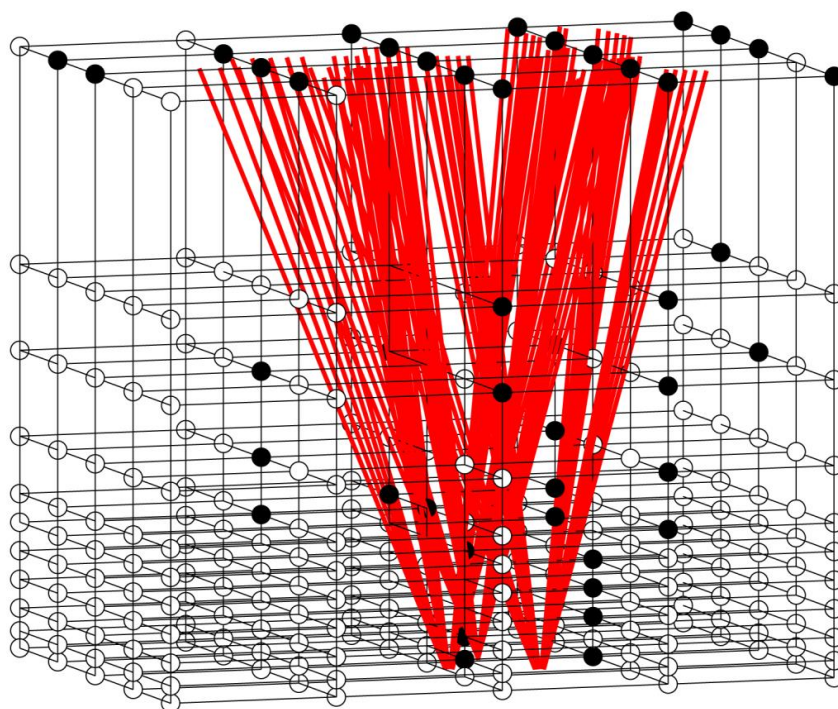
119 Voxel and node parameterization are the two common GNSS tomographic approaches. In
120 the former, the tomographic field, which is usually assumed as a rectangular cube, is divided into
121 many voxels (small rectangular cubes) and in the latter, and the field is discretized by nodes, as
122 all the black and circle nodes shown in Fig. 1. In this study, the node parameterization approach
123 was adopted due to its better fitting of the spatial correlation of water vapor.



124 In the current node parameterization approaches, if the GNSS network is very small, e.g.
125 a three-station network from the Hong Kong Satellite Positioning Reference Station
126 (SatRef) as shown in Fig. 1, a large number of nodes are in the ESR (see the hollow circles)
127 within the rectangular cube which is the tomographic field. These nodes, as part of the unknown
128 parameters, need to be estimated. The inclusion of these unknown parameters in the estimation
129 process does not only add more ‘redundant’ parameters but also degrades the accuracy of the
130 solution.

131

132

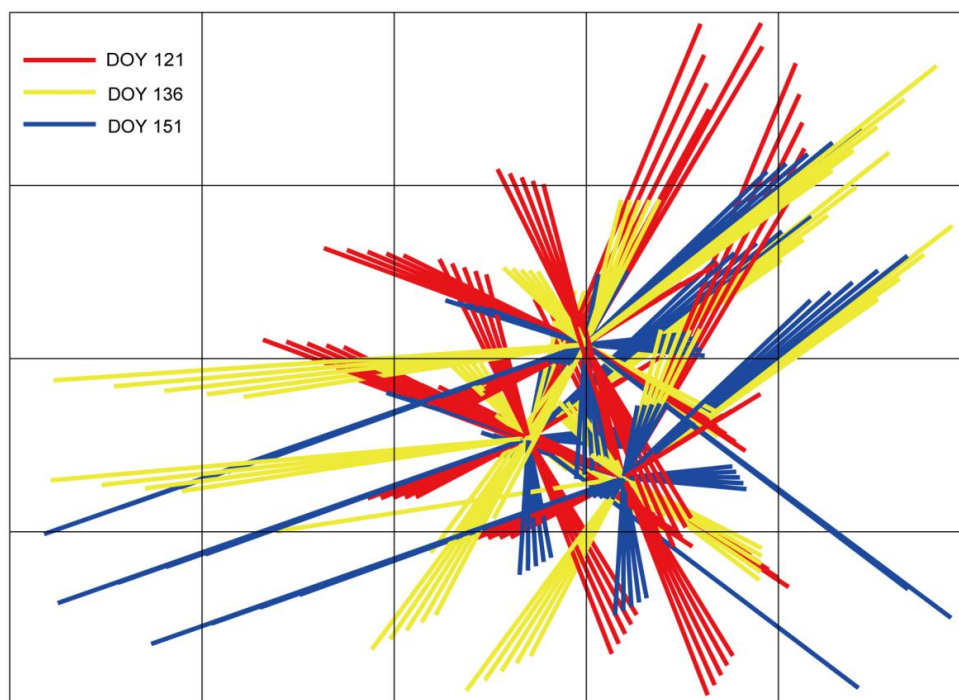


133

134 **Figure 1.** A three-station GNSS network from the Hong Kong Satellite Positioning Reference
135 Station Network (SatRef) as an example for GNSS tomography—the rectangular cube is the
136 tomographic field adopted in current node parameterization approaches, the solid nodes are those
137 near GNSS signals and the hollow nodes are those in the ESR.

138

139 In addition, a fixed rectangular cube is used as the tomographic field for all time in the
140 current approaches, In fact, the spatial region that the signals travel through varies with time, as
141 shown in Fig. 2 for the different distributions of the signals at the three stations shown in Fig. 1
142 on the top plane of the tomographic field at UTC 0 on 1 (day of year (DOY) 121), 16 (DOY 136)
143 and 31 (DOY 151) in May 2015.



144

145 **Figure 2.** Distributions of GNSS signals at the three stations shown in Fig. 1 on the top plane of
146 the tomographic field at UTC 0 on 1(DOY 121), 16 (DOY 136) and 31 (DOY 151) in May 2015.

147 To address the above issues, a new node parameterization approach that dynamically
148 adjusts the tomographic field based on the spatial distribution of the GNSS signals at the
149 tomographic epoch and also dynamically adjusts the location and number of all the nodes based
150 on the size of the tomographic field is proposed. Its procedure is elaborated in the next section.

151

152 2.2.2 New approach

153 The procedure for the new approach mainly includes two steps—determination of
154 tomographic field and determination of node position, which are introduced below.

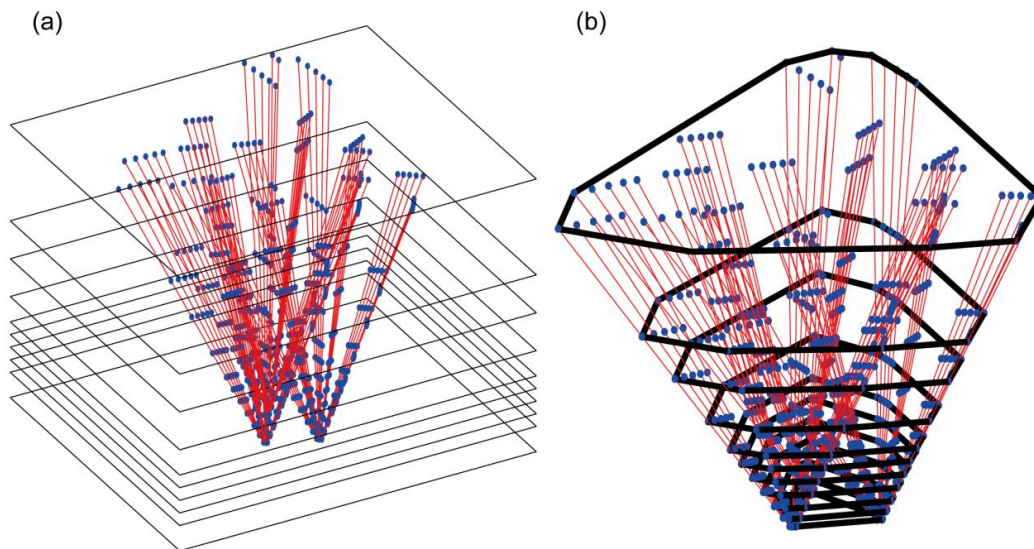
155 *i) Determination of tomographic field*

156 A tomographic field is regarded to be comprised of many layers in the vertical dimension
157 and these layers with the same or different thickness, depending on the distribution of water
158 vapor at the height of the layer, as shown in Fig. 3(a), each layer is formed by two neighboring
159 horizontal planes. After all these planes are determined, the next task is to determine the
160 tomographic boundary for each plane, according to the distribution of the GNSS signals on the
161 plane. Fig. 3(b) shows the tomographic boundary on each of the planes shown in Fig. 3(a), which
162 is determined from the following three steps that were used in the Graham scan (Graham, 1972)
163 determining all the intersections (the blue points) of the GNSS signal paths on the plane (they



164 are name pierce points in this paper); 2) using a stack of the pierce points to detect and remove
165 all those pierce points that are in concavities; and 3) connecting the rest pierce points to form a
166 convex hull, which is the tomographic boundary (black polygon).

167



168

169 **Figure 3.** (a) A tomographic field is divided by many layers, the thickness of which is dependent
170 upon the distribution of water vapor in the layer, the red lines are the sampling GNSS signals and
171 the blue points are the intersections of the GNSS signals on each horizontal plane; and (b)
172 Tomographic boundary is depicted by the black polygon on each horizontal plane.

173

174 Since the shape of the tomographic boundary determined using the new approach is irregular,
175 it is difficult to generate equidistant nodes within the boundary. This differs from current node
176 parameterization approaches in which uniformly distributed nodes can be easily pre-set. In this
177 study meshing techniques are used to adjust the position of nodes for each plane and each
178 tomographic epoch, and their procedure is discussed in the next section.

179 *ii) Determination of node position*

180 Meshing techniques for the generation of equidistant nodes of a GNSS tomographic
181 model include three steps and each of the steps is introduced below.

182 1) A mesh background in a desired size with nodes is used to provide initial nodes for
183 each plane see Fig. 4(a) where the polygon is obtained from the last section for the tomographic
184 boundary on the plane and at all the vertices of the polygon a new set of nodes are also attached
185 to the initial nodes, see Fig. 4(b) for the final initial nodes.

186 2) Delaunay triangulation (Delaunay, 1934) is used to establish a topology for the above
187 initial nodes on each plane. It determines non-overlapping triangles that fill the region in a
188 polygon such that every edge is shared by at most two triangles and none of the vertices is inside
189 the circumcircle of any of the triangles. Delaunay triangulations maximize the minimum angle of



190 all the triangles to avoid sliver triangles which has undesirable properties during some
191 interpolation or rasterization processes (Edelsbrunner et al., 2000). Several methods have been
192 developed to compute the Delaunay triangulation such as the commonly used flipping edges and
193 conversing a Voronoi diagram. In this study, the flipping edges method is adopted to connect the
194 initial nodes shown in Fig. 4(b) by the edges of Delaunay triangles on each plane and the
195 topology formed is shown in Fig. 4(c).

196 3) The force displacement algorithm (Persson, 2005) is applied to the above topology for
197 the adjustment of the initial nodes into equidistance with a reasonable length fitting the size of
198 the tomographic boundary on each plane. This method is based on the assumption that each edge
199 in the topology has a force value (let it be F_{ij}) equal to the length of the edge. It can be used to
200 make all the edges' F_{ij} close to the same and reasonable pre-set force value F_0 for a (roughly)
201 regularly distributed mesh. This is the main reason for the introducing of this method to this
202 study for adjusting the nodes in the irregular tomographic boundary (like Fig. 4(c)) into
203 equidistance (roughly). The force displacement algorithm is an iterative process as:

$$204 \quad [X^k \quad Y^k] = [X^{k-1} \quad Y^{k-1}] + Scal \cdot [F_x^k \quad F_y^k] \quad (2)$$

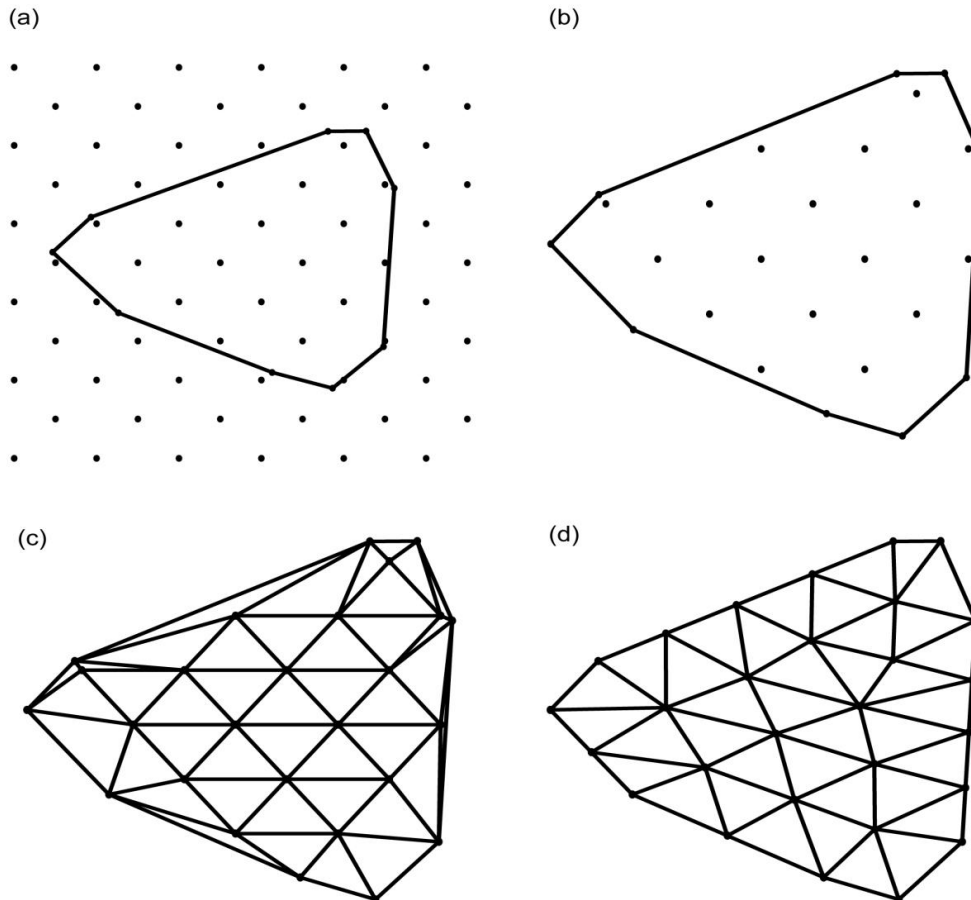
205 where X^k and Y^k are the vectors of the x and y coordinates respectively of all the nodes on the
206 plane at the k th iteration and $k-1$ denotes the previous iteration; $Scal$ is a relaxation factor for
207 constraining the amount of the movement from the $k-1$ th iteration to an appropriate value, for
208 which a 0.2 value is commonly used; F_x^k is the vector of the vector sums of all the forces
209 working on each of the nodes in the x direction, F_y^k is that in the y direction.

210 After the above algorithm is performed, all the nodes on the plane can be adjusted from
211 the initial position (Fig. 4(c)) to equidistant position (Fig. 4(d)) through a series of iterations.

212 It is noted that the sizes of the tomographic boundaries on different planes are different
213 (Fig. 3(b)) while the numbers of the signals on different planes are the same, so the densities of
214 the signals on different planes are different, and the densities of the nodes on different planes
215 better be different through using different F_0 values. In this study, the F_0 value for the i th plane is
216 calculated by:

$$217 \quad F_0^i = C \cdot \text{mean}(Ls^i) \quad (3)$$

218 where C is a constant coefficient and 0.68 is adopted for all planes; and $\text{mean}(Ls^i)$ is the mean of
219 all the lengths of the edges on the polygon.
220



221

222 **Figure 4.** (a) Two sets of nodes for initialization—one set is generated using a mesh background
 223 with a desired size which is usually slightly larger than the region of the GNSS signals at all time
 224 and the other set is at all the vertices of the polygon (all black points); (b) Initial nodes; (c)
 225 Topology formed using Delaunay triangulation; (d) Nodes with equidistance adjusted based on
 226 the force displacement algorithm.

227 2.3 Observation equations

228 After equidistant nodes for all planes are determined (like Fig. 4(d)), the next step is to
 229 estimate water vapor parameters at these nodes from observation equations of GNSS-derived
 230 *SWDs*. The derivation of the observation equations is as follows.

231 Theoretically, *SWD* is defined as the integral of wet refractivity N_w along the signal path s

$$232 \quad \text{SWD} = 10^{-6} \cdot \int_s N_w ds \quad (4)$$

233 It can be further decomposed into integrations of n layers:



234

$$SWD = \sum_{i=1}^n \int_{s_i}^{s_{i+1}} N_w^s(i) ds = \sum_{i=1}^n SWD_i \quad (5)$$

235
 236

where $N_w^s(i)$ is wet refractivity in the i th layer; s_i, s_{i+1} are the start and end points of the layer/integral; and SWD_i is the part of the SWD in the i th layer

237
 238
 239
 240
 241
 242
 243

In GNSS tomography, in each of the piecewise integrals expressed in Eq. (5), i.e. SWD_i , the signal path in the layer is further divided into several equally spaced points and then SWD_i is approximated as a function of wet refractivity at these points using the Newton-Cotes formulae (Perler et al., 2011). In this study, SWD_i is approximated by the Newton-Cotes formulae of 4 degree at five equally spaced points, as (P_1, \dots, P_5) shown in Fig. 5 where the plane i and plane ($i+1$) are the two horizontal planes corresponding to the above s_i, s_{i+1} respectively, and the black solid dots denote some of the equidistant nodes obtained from Fig. 4(d).

244

The methods for obtaining wet refractivity at each of the points are as follows.

245
 246
 247

i) Wet refractivity at points P_1 and P_5 (which are on the i th and ($i+1$)th planes respectively) can be calculated using the interpolation method of the inverse-distance-weighted (IDW) mean of the sample wet refractivity data from its surrounding nodes:

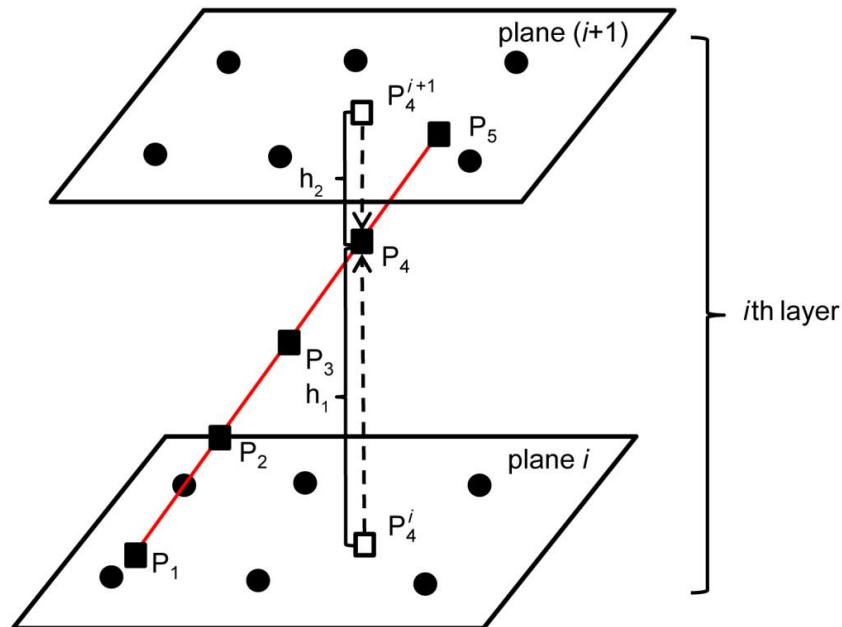
248

$$P_{wet} = \frac{\sum_{j=1}^m w_j \cdot n_j^{wet}}{\sum_{j=1}^m w_j} \quad (6)$$

249
 250

where j is the index of the sample data, and w_j is its weight determined by the inverse-distance; and m is the number of the sample data.

251





252 **Figure 5.** Five equally spaced points (black solid squares) for an approximation of wet
 253 refractivity for the i th layer. P_4^i and P_4^{i+1} (black hollow squares) are the projected points of P_4 on
 254 the i th and $(i+1)$ th planes respectively, h_1 is the height difference between P_4 and P_4^i , and h_2 is
 255 that between P_4 and P_4^{i+1} .

256 ii) Wet refractivity at points P_2 , P_3 and P_4 , cannot be directly interpolated like that for P_1
 257 and P_5 , the following three-step procedure needs to be performed (P_4 is taken as an example): 1)
 258 the position of P_4 is projected onto both the i th and $(i+1)$ th planes to obtain two projected points
 259 named P_4^i and P_4^{i+1} , respectively; 2) the above interpolation procedure for P_1 and P_5 is used to
 260 obtain wet refractivity P_{4wet}^i and P_{4wet}^{i+1} at P_4^i and P_4^{i+1} respectively; and 3) P_{4wet}^i and P_{4wet}^{i+1} are used to
 261 obtain a weighed mean wet refractivity for the position of P_4 using [Reitan, 1963; Tomasi, 1981]:

$$262 \quad P_4 = \frac{|h_1|}{(|h_1| + |h_2|)} P_{4wet}^i \cdot e^{-h_1/H} + \frac{|h_2|}{(|h_1| + |h_2|)} P_{4wet}^{i+1} \cdot e^{-h_2/H} \quad (7)$$

263 where h_1 is the height difference between P_4 and P_4^i and h_2 is that between P_4 and P_4^{i+1} ; and H is
 264 water vapor scale height, which can be calculated by Tomasi [1977]:

$$265 \quad H = \frac{10W}{\rho_s} \quad (8)$$

266 where W and ρ_s are the vertical total water vapor content (in g m^{-2}) and surface humidity (in g m^{-3})
 267 respectively, and both can be obtained from GNSS data.

268

269 After the above procedures are carried out, SWD_i can be expressed as a function of wet
 270 refractivity at a set of nodes. This procedure needs to be performed for all SWD_i ($i=1,2,..,n$), then
 271 the next step is to substitute these SWD_i expressions and the SWD observation into Eq. (5), to
 272 form its GNSS tomographic observation equation.

273 The final GNSS tomographic observation equations of all SWD s from the GNSS network
 274 for the tomographic modeling is expressed as:

$$275 \quad A \cdot X = b \quad (9)$$

276 where A is the coefficient matrix of the model; b is the vector of the SWD observations; and X is
 277 the vector of the wet refractivity parameters at all nodes.

278 The X vector in Eq. (9) can be estimated using the least squares method. However, due to
 279 the problem with the sparseness of A , the algebraic reconstruction technique (ART) was used to
 280 estimate X in this study.

281 2.4 Tomographic solution

282 The ART has been successfully applied to reconstruction of water vapor field (Chen and
 283 Liu, 2014; Bender et al., 2011). Its main advantage is the high numerical stability, even under
 284 adverse conditions and also relatively easy to incorporate prior knowledge into the reconstruction
 285 process. The ART used to solve Eq. (9) is (Kaczmarz, 1937):

$$286 \quad x^{k+1} = x^k + \lambda \frac{b_i - \langle a_i, x^k \rangle}{\|a_i\|_2^2} a_i \quad i = 1, 2, \dots, m \quad (10)$$



287 where a_i and b_i denote the i th rows in A and b respectively; x_k is the k th iterative solution; and λ is
 288 a relaxation factor and the value of 0.2 was selected in this study.

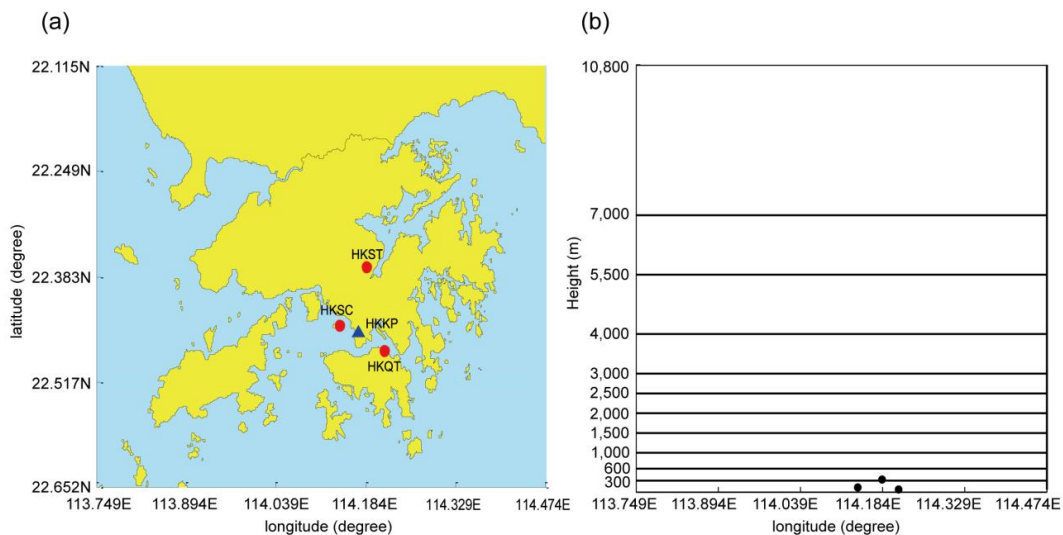
289 It is noted that Eq. (9) needs to be sorted in a certain sequence for Eq. (10). This is
 290 different from the commonly used observation equation system in which the order of the
 291 observation equations is not a matter. In this study, an access order scheme based on prime
 292 number decomposition (PND) proposed in (Ding et al., 2017) was used for the ordering of the
 293 observation equations such that the observation equations between two consecutive iterations are
 294 largely uncorrelated.

295 The unknown parameters X solved from Eq. (10) are the wet refractivity values at all
 296 tomographic nodes. In some meteorological applications, water vapor density may be preferred,
 297 in this case X needs to be converted using a conversion factor I which is a function of water-
 298 vapor-weighted-mean temperature T_m (Bevis et al., 1994; Wang et al., 2016) at the position of
 299 the nodes.

300 3 Test results

301 3.1 Data selection and tomographic scheme

302 Test data used in this study were from three stations in the Hong Kong Satellite
 303 Positioning Reference Station Network (SatRef), and the horizontal and vertical distributions of
 304 the three stations are presented in Fig. 6(a) and Fig. 6(b), respectively. The area of our interest
 305 ranges from 113.749 °E to 114.474 °E in the longitudinal direction, from 22.115 °N to 22.651 °N
 306 in the latitudinal direction and from 0 to 10800 m in the vertical direction. Radiosonde data from
 307 King's Park Meteorological Station (HKKP) (the blue triangle shown in Fig. 6(a) were used as
 308 the reference for the validation of our test results.



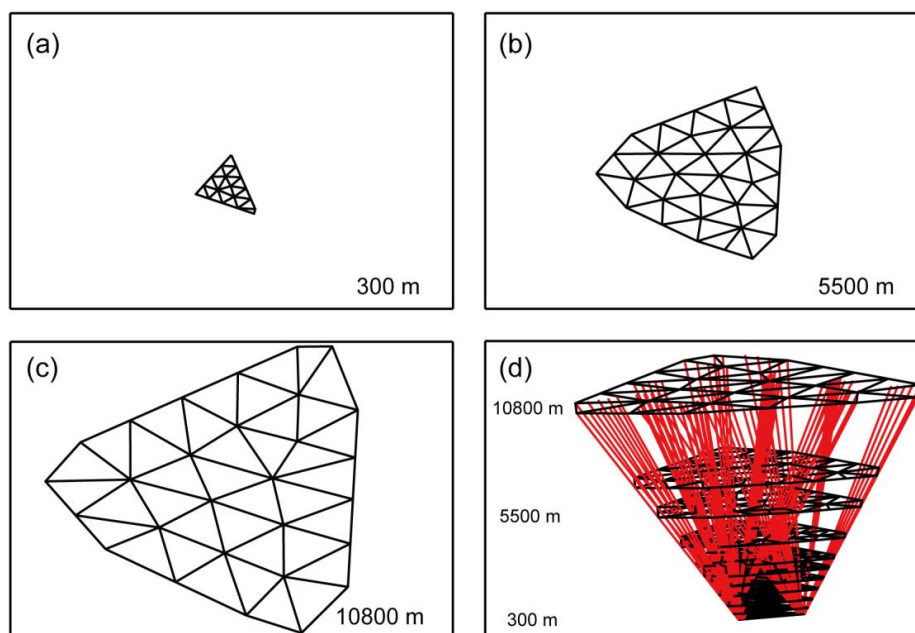
309
 310 **Figure 6.** (a) Horizontal distribution of the three stations selected from the Hong Kong reference
 311 stations (red dots) and HKKP (blue triangle); and (b) Vertical distribution of the three stations
 312 (black spots) and vertical layers used in tomographic modeling.



313 The test data were from the whole month of May, 2015 (day of year (DOY) 121–151)
314 with the sampling rate of 30 seconds, and the GAMIT software was used to obtain SWDs at the
315 same rate in the data processing. For the tomographic modeling, a 5-minute sampling rate for
316 SWDs and a 30-minute interval for a tomographic epoch were adopted, meaning that the number
317 of SWD observations for a tomographic epoch was seven—including the two sample data at the
318 two ends of the interval. The reason for the selection of data from May 2015 is that its monthly
319 total rainfall was 513.0 mm, a 68% larger than the normal level of 304.7 mm.

320 The tomographic scheme for testing is as follows. The first step is to determine the
321 vertical planes/layers for the tomographic field. Non-uniform vertical intervals from 300 to 3800
322 m (Fig. 6(b)) were selected for adaption to the inherent characteristic of water vapor spatial
323 distribution—it exponentially decreases with the increase of height. The use of this structure can
324 also avoid too many unknown parameters overfitting the SWD observations. The next step is to
325 determine the tomographic polygon/boundary on each of the above planes using the methods in
326 section 2.2.1 and based on the GNSS signals in the tomographic interval, then according to the
327 polygon's perimeter, a F_0 value in the force displacement algorithm for determination of the
328 density of nodes on each plane is calculated. All F_0 results in our test are in the range of about
329 1800–10000 m corresponding to the range of height 300–10800 m. The position of the nodes on
330 each plane is determined by Eq. (2).

331 Figure 7 shows the boundary and nodes on three tomographic planes at tomographic
332 epoch UTC 0 on DOY 121, 2015 for an example. Tomographic model results are presented in
333 the next section.



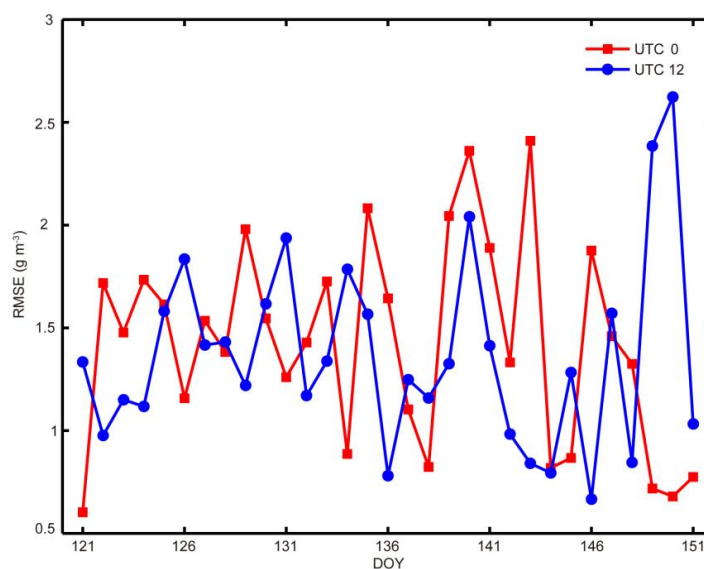
334

335 **Figure 7.** Tomographic boundary and nodes on three planes ((a), (b) and (c)) and the
336 tomographic field and nodes (d) at tomographic epoch UTC 0 on DOY 121, 2015.



337 3.2 Results of profiles

338 Water vapor density values obtained from the tomographic models at tomographic
339 epochs UTC 0 and UTC 12 on each day of the month (DOYs 121–151) were compared against
340 radiosonde (RS) data for evaluation of the model's accuracy. The values of the tomographic
341 results at all RS sampling points were calculated first using the interpolation method mentioned
342 in section 2.2.1, then the root mean square error (RMSE) of the differences between the
343 interpolated values and RS observations at all the sampling points of the RS profile from the
344 ground surface to 10800 m at each epoch was calculated for the accuracy of the profile. All the
345 results at the 62 epochs during the 31-day period are shown in Fig. 8.



346

347

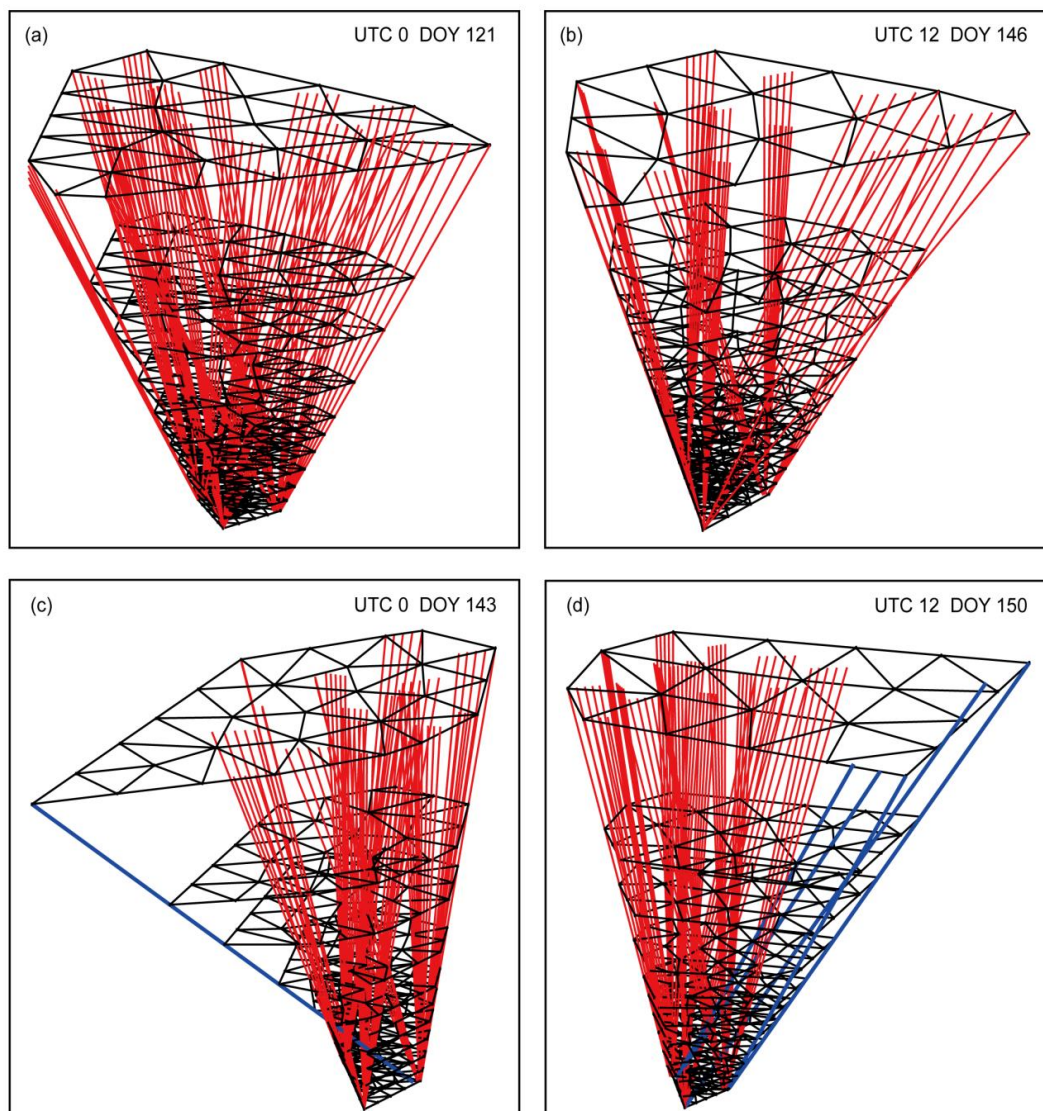
348 **Figure 8.** RMSE of model-derived water vapor density values at all RS sampling points of the
349 RS profile below 10800 m at tomographic epochs UTC 0 and UTC 12 on each day of the month
350 (DOYs 121–151).

351

352 The maximum RMSEs, i.e., the worst results, at UTC 0 (red) and UTC 12 (blue) are on
353 DOY 143 and DOY 150 respectively; while the best result (the minimum RMSEs) at the two
354 epochs are on DOYs 121 and 146. In order to find the reason for the large difference between the
355 worst and best results, the tomographic field, the distribution of the signals and the nodes at these
356 four epochs are given in Fig. 9, where Fig. 9(a) and Fig. 9(b) correspond to the best results at
357 UTC 0 and UTC 12 respectively, both of which show uniform distributions of the GNSS signals.
358 However, the distributions of the GNSS signals corresponding to the worst results at UTC 0 (Fig
359 9(c)) and UTC 12 (Fig 9(d)) are different in the sparse signals shown in blue lines, which is the
360 reason for the poor accuracy of the model results.

361

362



363

364 **Figure 9.** Tomographic field and signal distribution at tomographic epoch UTC 0 on DOY 121
365 (a), UTC 12 on DOY 146 (b), UTC 0 on DOY 143 (c), and UTC 12 on DOY 150 (d).

366 The results shown in Fig. 8 are the statistics of the model results for each epoch on each
367 day. The statistics of the model results at both epochs together in the whole month are presented
368 in Table 1. The three values listed in the table are all small, meaning that the new approach for a
369 few GNSS stations, such as three stations, is feasible.

370

371



372 **Table 1.** Monthly statistics of tomographic modeling results

373

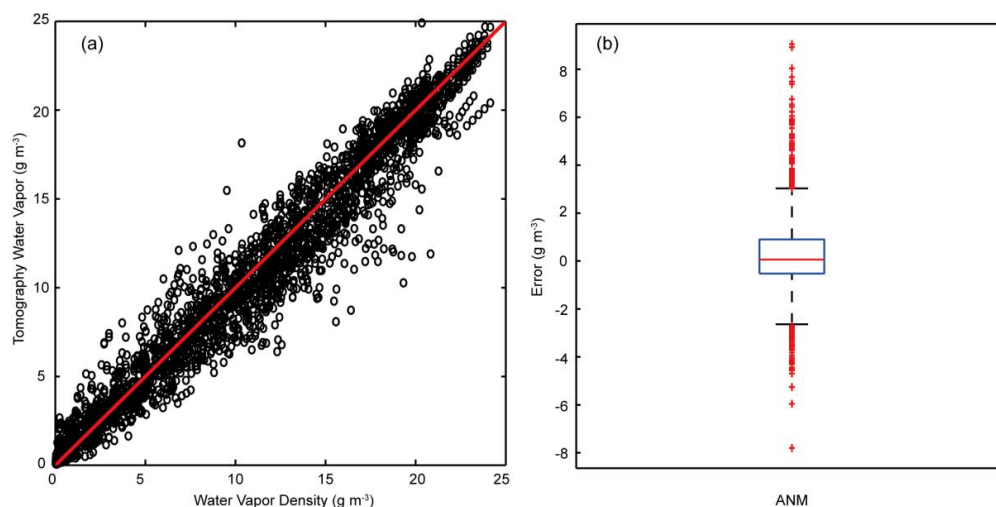
Statistic	RMSE (g m^{-3})	Bias (g m^{-3})	IQR (g m^{-3})
	1.477	0.239	1.430

374

375 To indicate the spread of all the errors (the ones used to calculate the above monthly
 376 statistics), scatter plots shown in Fig. 10(a) are used to analyze the characteristics of these errors
 377 in different intervals. The x and y axes denote the RS observation and the model result (in g m^{-3})
 378 respectively; each hollow circle corresponds to a sampling point's result; and the red line
 379 represents the “perfect” results, i.e. the model results equal to the RS results. Those hollow
 380 circles that are on the red line have an error value of zero, those above the red line have a
 381 positive error value, and the rest have a negative error value. The closer a hollow circle to the red
 382 line, the smaller its error value.

383 How well all the hollow circles “fit” the red line indicates the overall quality of the model
 384 results. It is clear that the hollow circles have a cigar-shaped (fusiform) distribution. The hollow
 385 circles in both ending intervals ($[0-5]$ and $[20-25]$ g m^{-3}) more concentrate around the red line
 386 than those in the middle part ($[5-20]$ g m^{-3}). The reason for this is 1) most of the sampling points
 387 in the $[20-25]$ g m^{-3} interval are located near the ground surface, where water vapor density
 388 decreases exponentially with the increase of height and the density of the GNSS signals is very
 389 high, resulting in relative high accuracy; 2) most of the sampling points in the $[5-20]$ g m^{-3}
 390 interval are located in the mid-height of the tomographic field, where the GNSS signals are
 391 sparser than the $[20-25]$ g m^{-3} interval, leading to a larger tomographic field, which results in a
 392 lower accuracy; and 3) most of the sampling points in the $[0-5]$ interval are located in the top
 393 section of the tomographic field, where the water vapor values are smaller than the other two
 394 intervals, leading to the smallest errors.

395



396



397 **Figure 10.** Graphic presentation for the distribution of the tomographic results at the two epochs
 398 on every day during the month: (a) scatter plot of water vapor density; and (b) box plot for
 399 outlier detection of the tomographic errors.

400 The box plot is mainly for the indication of those large errors at all sampling points. Q1
 401 and Q3, which are the first and third quartiles respectively, determine the IQR value in Table 1;
 402 Q2, the second quartile, roughly reflects the bias of all the errors; the whiskers, i.e. the two black
 403 bars, located at $Q1-1.5(IQR)$ and $Q3+1.5(IQR)$, are for the determination of the lower and upper
 404 bounds of the criteria for outlier detection, e.g. the red cross marks are regarded outliers. Table 2
 405 lists all the above characteristic values.

406

407 **Table 2.** Characteristic values of the box plots in Fig. 10(b).

408

Statistic	Q1 (g m^{-3})	Q2 (g m^{-3})	Q3 (g m^{-3})	Upper bound (g m^{-3})	Lower bound (g m^{-3})	Number of outliers
	-0.527	0.062	0.903	3.048	-2.672	159

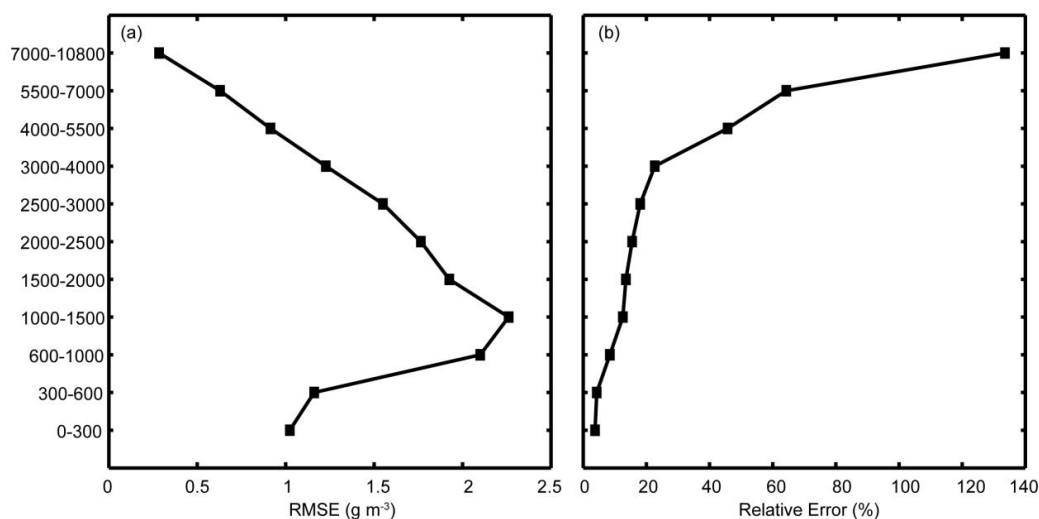
409

410 3.3 Results of different layers

411 In the last section, the RMSE of model-derived water vapor density values at all sampling
 412 points for each profile (Fig. 8) and the errors at all the sampling points and two epochs on each
 413 day during the month (Fig. 9) are analyzed for the assessment of the overall performance of the
 414 models. In this section, the monthly RMSE at all the sampling points but in 11 different
 415 tomographic layers and the monthly mean of the relative errors in these layers are investigated,
 416 see Fig. 11.

417 In those layers below 1500 m, the two lines in both subfigures show the same tendency of
 418 variation with height –the error value increases with the increase of height. This is because the
 419 higher the layer, the more the spread of the GNSS signals, the worse the accuracy of the result.
 420 However, in the layers above 1500 m, the two lines show opposite tendencies of variation with
 421 height because the higher, the smaller the water vapor density. The smaller water vapor density
 422 values in these high layers lead to the small RMSE and large relative errors.

423



424

425 **Figure 11.** (a) Monthly RMSE of (absolute) tomographic errors and (b) mean of relative
426 tomographic errors in different layers.

427 **4 Conclusion and outlook**

428 In this study a new node parameterization approach for determination of a tomographic
429 field based on the distribution of GNSS signals at the tomographic epoch and also for
430 discretization of the tomographic field is proposed. The number and the position of the nodes on
431 each tomographic plane are determined based on the perimeter of the tomographic boundary on
432 the plane and meshing techniques respectively. Since the tomographic model is tailor-made for
433 the tomographic field at the epoch, the new approach is applicable to not only GNSS networks
434 with several stations, but also GNSS networks with few stations, e.g., three stations, which
435 cannot be solved by conventional approaches. The new approach was tested using GNSS data
436 from three stations in the Hong Kong Satellite Positioning Reference Station Network during the
437 period of May, 2015 and its model results were validated by comparing them against radiosonde
438 data at UTC 0 and UTC 12 from HKKP. Results suggest that the new approach is feasible for a
439 three-station GNSS network. In addition, monthly statistics of the tomographic results on each
440 tomographic layer indicated that the size of the tomographic boundary and the magnitude of
441 water vapor are two critical factors affecting the accuracy of the tomographic result of the layer.

442 Our future work will be focusing on using unevenly distributed nodes that fit the density
443 of the GNSS signals.

444 **Acknowledgements**

445 This study is supported by the National Natural Science Foundation of China (No.
446 41730109), the National Natural Science Foundation of China (No. 41774026). The authors
447 acknowledge the Survey and Mapping Office (SMO) of Lands Department, Hong Kong for
448 provision of GNSS data from the Hong Kong Satellite Positioning Reference Station Network
449 (SatRef). We also thank King's Park Observatory for provision of radiosonde data, and the
450 Department of Earth Atmospheric and Planetary Sciences, MIT for the GAMIT/GLOBK



451 software. The editor and reviewer team is also highly appreciated for their valuable comments,
452 which makes great improvements in the quality of the paper.

453

454 **Data availability**

455 GNSS data in the RINEX format used for this study can be downloaded from website
456 (<http://www.geodetic.gov.hk/smo/gsi/programs/en/GSS/satref/satref.htm>). Radiosonde data of
457 King's Park Meteorological Station can be downloaded from website
458 (<http://weather.uwyo.edu/upperair/sounding.html>).

459

460 **Competing interests**

461 The authors do not have any possible conflicts of interest.

462

463 **References**

- 464 Bastin, S., Champollion, D., Bock, O., Drobinski, P., and Masson, F.: On the use of GPS
465 tomography to investigate water vapor variability during a Mistral/sea breeze event in
466 southeastern France, *GEOPHYS. RES. LETT.*, 32, 2005.
- 467 Bender, M., Dick, G., Wickert, J., Ramatschi, M., Ge, M., Gendt, G., Rothacher, M., Raabe, A.,
468 and Tetzlaff, G.: Estimates of the information provided by GPS slant data observed in
469 Germany regarding tomographic applications, *J. GEOPHYS. RES.*, 114, 2009.
- 470 Bender, M., Stosius, R., Zus, F., Dick, G., Wickert, J., and Raabe, A.: GNSS water vapour
471 tomography – Expected improvements by combining GPS, GLONASS and Galileo
472 observations, *ADV. SPACE. RES.*, 47, 886-897, 2011.
- 473 Bevis, M., Businger, S., Chiswell, S., Herring, T. A., Anthes, R. A., Rocken, C., and Ware, R. H.:
474 GPS meteorology: Mapping zenith wet delays onto precipitable water, *J. APPL.*
475 *METEOROL.*, 33, 379-386, 1994.
- 476 Champollion, C., Masson, F., Bouin, M. N., Walpersdorf, A., Doerflinger, E., Bock, O., and Van
477 Baelen, J.: GPS water vapour tomography: preliminary results from the ESCOMPTE
478 field experiment, *ATMOS. RES.*, 74, 253-274, 2005.
- 479 Chen, B., and Liu, Z.: Voxel-optimized regional water vapor tomography and comparison with
480 radiosonde and numerical weather model, *J. GEODESY.*, 88, 691-703, 2014.
- 481 Chen, B., Liu, Z., Wong, W., and Woo, W.: Detecting Water Vapor Variability during Heavy
482 Precipitation Events in Hong Kong Using the GPS Tomographic Technique, *J. ATMOS.*
483 *OCEAN. TECH.*, 34, 1001-1019, 2017.
- 484 Delaunay, B. N.: Sur la Sphere Vide, *Izv.akad.nauk Sssr*, 7, 793-800, 1934.
- 485 Ding, N., Zhang, S., and Zhang, Q.: New parameterized model for GPS water vapor tomography,
486 *ANGEOS.*, 35, 311-323, 2017.



- 487 Edelsbrunner, H., Li, X. Y., Miller, G., Stathopoulos, A., Talmor, D., Teng, S. H., Üng R, A.,
488 and Walkington, N.: Smoothing and cleaning up slivers. ACM Symposium on Theory of
489 Computing, 2000.
- 490 Flores, A., Ruffini, G., and Rius, A.: 4D tropospheric tomography using GPS slant wet delays,
491 ANN. GEOPHYS-ATM. HYDR., 18, 223-234, 2000.
- 492 Gradinarsky, L. P.: Sensing atmospheric water vapor using radio waves, Chalmers University of
493 Technology, 90-106, 2002.
- 494 Gradinarsky, L. P., and Jarlemark, P.: Ground-based GPS tomography of water vapor: Analysis
495 of simulated and real data, J. METEOROL. SOC. JPN., 82, 551-560, 2004.
- 496 Graham, R. L.: An efficient algorithm for determining the convex hull of a finite planar set,
497 INFORM. PROCESS. LETT., 4(1), 132–133, 1972.
- 498 Hoyle, V. A.: Data assimilation for 4-D wet refractivity modelling in a regional GPS network,
499 University of Calgary, Department of Geomatics Engineering, 139–150, 2005.
- 500 Kaczmarz, S.: Angen äherte aufl ösung von systemen linearer gleichungen, Bulletin International
501 de l’Academie Polonaise des Sciences et des Lettres, 35, 355-357, 1937.
- 502 Perler, D., Geiger, A., and Hurter, F.: 4D GPS water vapor tomography: new parameterized
503 approaches, J. GEODESY., 85, 539-550, 2011.
- 504 Persson, P.: Mesh generation for implicit geometries, Massachusetts Institute of Technology,
505 2005.
- 506 Rohm, W., and Bosy, J.: Local tomography troposphere model over mountains area, ATMOS.
507 RES., 93, 777-783, 2009.
- 508 Rohm, W., Zhang, K., and Bosy, J.: Limited constraint, robust Kalman filtering for GNSS
509 troposphere tomography, ATMOS. MEAS. TECH., 7, 1475-1486, 2014.
- 510 Saastamoinen, J.: Atmospheric correction for the troposphere and stratosphere in radio ranging
511 satellites, The use of artificial satellites for geodesy, 247-251, 1972.
- 512 Seko, H., Shimada, S., Nakamura, H., and Kato, T.: Three-dimensional distribution of water
513 vapor estimated from tropospheric delay of GPS data in a mesoscale precipitation system
514 of the Baiu front, EARTH PLANETS. SPACE., 52, 927-933, 2000.
- 515 Troller, M., Geiger, A., Brockmann, E., Bettems, J. M., Burki, B., and Kahle, H. G.:
516 Tomographic determination of the spatial distribution of water vapor using GPS
517 observations. In: Burrows, J. P., Eichmann, K. U., and LLewellyn, E. J., ASR., 2006.
- 518 Wang, X., Zhang, K., Wu, S., Fan, S., and Cheng, Y.: Water vapor - weighted mean temperature
519 and its impact on the determination of precipitable water vapor and its linear trend, J.
520 GEOPHYS. RES-ATMOS., 121, 833-851, 2016.
- 521 Wang, X., Zhang, K., Wu, S., He, C., Cheng, Y., and Li, X.: Determination of zenith hydrostatic
522 delays and the development of new global long-term GNSS-derived precipitable water
523 vapor, ATMOS. MEAS. TECH., 1-17, 2017.
- 524 Xia, P., Cai, C., and Liu, Z.: GNSS troposphere tomography based on two-step reconstructions
525 using GPS observations and COSMIC profiles. ANGIO., Copernicus GmbH, 2013.



- 526 Yao, Y. B., Zhao, Q. Z., and Zhang, B.: A method to improve the utilization of GNSS
527 observation for water vapor tomography, ANN. GEOPHYS-GERMANY., 34, 143-152,
528 2016.
- 529 Ye, S., Xia, P., and Cai, C.: Optimization of GPS water vapor tomography technique with
530 radiosonde and COSMIC historical data, 34, ANGIO., 789-799, 2016.
- 531 Zhang, K., Manning, T., Wu, S., Rohm, W., Silcock, D., and Choy, S.: Capturing the Signature
532 of Severe Weather Events in Australia Using GPS Measurements, IEEE. J-STARS., 8,
533 1839-1847, 2015.